Chemical Science

ROYAL SOCIETY OF CHEMISTRY

EDGE ARTICLE

View Article Online
View Journal | View Issue

Cite this: *Chem. Sci.*, 2023, **14**, 10167

All publication charges for this article have been paid for by the Royal Society of Chemistry

Received 16th May 2023
Accepted 31st August 2023

DOI: 10.1039/d3sc02493h

rsc.li/chemical-science

Versatile synthesis of nano-icosapods *via* cation exchange for effective photocatalytic conversion of biomass-relevant alcohols†

Dan Xu,‡[a] Li Zhai,‡[ac] Zhangyan Mu,[a] Chen-Lei Tao,[a] Feiyue Ge,[a] Han Zhang,[b] Mengning Ding,[a] Fang Cheng*[b] and Xue-Jun Wu*[a]

Branched metal chalcogenide nanostructures with well-defined composition and configuration are appealing photocatalysts for solar-driven organic transformations. However, precise design and controlled synthesis of such nanostructures still remain a great challenge. Herein, we report the construction of a variety of highly symmetrical metal sulfides and heterostructured icosapods based on them, in which twenty branches were radially grown in spatially ordered arrangement, with a high degree of structure homogeneity. Impressively, the as-obtained CdS–Pd_xS icosapods manifest a significantly improved photocatalytic activity for the selective oxidation of biomass-relevant alcohols into corresponding aldehydes coupled with H_2 evolution under visible-light irradiation (>420 nm), and the apparent quantum yield of the benzyl alcohol reforming can be achieved as high as 31.4% at 420 nm. The photoreforming process over the CdS–Pd_xS icosapods is found to be directly triggered by the photogenerated electrons and holes without participation of radicals. The enhanced photocatalytic performance is attributed to the fast charge separation and abundant active sites originating from the well-defined configuration and spatial organization of the components in the branched heterostructures.

Introduction

Exploiting solar-energy-driven organic transformations *via* artificial photosynthesis, *e.g.,* selective oxidation of biomass-relevant alcohols, reduction of nitroaromatics and oxidation coupling of amines, for the production of value-added chemicals has attracted widespread attention in recent years, as it provides an alternative to replace fossil fuels, thus achieving the goal of carbon neutrality.[1–10] Developing an efficient artificial photocatalyst with outstanding performance is the key toward this goal. Among various photocatalytic materials, colloidal metal chalcogenide semiconductor-based nanomaterials have shown great priorities toward these photoreforming reactions due to their large molar extinction coefficients, adjustable band edge positions and rapid carrier migration capabilities.[11–18] For example, CdS nanostructures modified with a Ni cocatalyst could efficiently transform alcohols into corresponding aldehydes/ketones or selectively oxidize 5-hydroxymethylfurfural (HMF) to tunable products under visible light irradiation.[19,20] However, it is still challenging to achieve desired photocatalytic performance with high conversion and excellent selectivity.[21–25] Firstly, conventional architectures, such as core@shell, Janus, and dumbbell nanostructures, often suffer from fast charge recombination, poor surface passivation and slow oxidation-reduction kinetics, ultimately impeding their photocatalytic conversion rate.[26–28] Secondly, many patchy semiconductor-cocatalyst systems and hierarchical heterostructures already exhibit promising results, but the randomly arranged components and unclear interfaces in these structures make it difficult to reveal structure–property correlation.[29–35] Hence, delicate engineering of favorable metal chalcogenide-based photocatalysts with controlled morphology and configuration as well as a well-defined interface would be a powerful strategy to enhance their performance but it has not yet been realized.

Highly symmetrical branched metal chalcogenide nanostructures, featuring well-defined morphology and spatial organization, have been widely studied and showed versatile applications in photocatalysis, energy storage and conversion.[36–40] Compared with conventional colloidal metal chalcogenides, they exhibit distinct advantages originating from their unique architecture, *i.e.,* high-density branches with adjustable length would be beneficial for light absorption/

[a]*State Key Laboratory of Coordination Chemistry, School of Chemistry and Chemical Engineering, Nanjing University, Nanjing 210023, China. E-mail: xjwu@nju.edu.cn*

[b]*State Key Laboratory for Organic Electronics and Information Displays & Jiangsu Key Laboratory for Biosensors, Institute of Advanced Materials (IAM), Jiangsu National Synergetic Innovation Center for Advanced Materials (SICAM), Nanjing University of Posts and Telecommunications, Nanjing 210023, China. E-mail: iamfcheng@njupt.edu.cn*

[c]*Department of Chemistry, City University of Hong Kong, Tat Chee Avenue, Kowloon, Hong Kong, China*

† Electronic supplementary information (ESI) available. See DOI: https://doi.org/10.1039/d3sc02493h

‡ These authors contributed equally to this work.

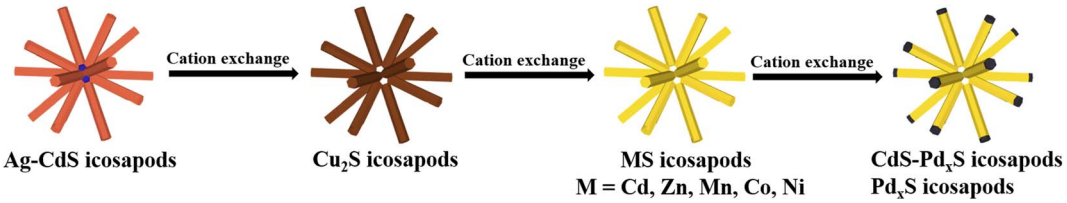

Scheme 1 Schematic illustration for the preparation of a variety of icosapods with tunable compositions by consecutive cation exchange.

scattering and charge separation/transport. Moreover, large specific surface area of such branches would provide abundant active sites, and accessible and interconnected networks in these nanostructures can promote the transport of guest organic species to accessible reaction sites. Therefore, it can be expected that highly symmetrical branched nanostructures could be an optimal architecture for improving activity toward photocatalytic organic transformations.[41–45] However, prototypical branched metal chalcogenide nanostructures are mainly tetrapods and octapods, and other types of highly branched nanostructures with more complicated symmetries have been rarely reported.[46,47]

Recently, we have reported the successful synthesis of a new type of highly symmetrical branched nanostructure, Ag–CdS icosapods, in which twenty CdS nanorods were radially grown on the [111] facets of multi-twinned Ag icosahedra.[48] In this work, highly symmetrical branched nanostructures with tunable compositions have been controllably synthesized *via* consecutive cation exchange by using Ag–CdS icosapods as templates (Scheme 1). First, Cu_2S icosapods were obtained by the cation exchange of the as-prepared Ag–CdS icosapods with cuprous ions, accompanied by the removal of Ag cores to form hollow cavities. Subsequently, a series of highly monodisperse and uniform metal sulfide icosapods (MS, M = Cd, Zn, Mn, Co, and Ni) can be obtained by using Cu_2S icosapods as templates for secondary cation exchange. Furthermore, Pd_xS icosapods and CdS–Pd_xS heterostructured icosapods with amorphous Pd_xS tips can also be produced. Interestingly, the as-prepared CdS–Pd_xS icosapods show excellent performance for visible light-induced biomass-relevant alcohol reformation (Sel. >94.8%) integrated with H_2 evolution compared with blank CdS icosapods and their other counterparts. The apparent quantum yield (AQY) of the benzyl alcohol (BA) reforming on CdS–Pd_xS icosapods is measured to be as high as 31.4% at 420 nm. *In-situ* electron paramagnetic resonance (EPR) and reactive species trapping experiments indicate that the photoreforming process over the CdS–Pd_xS icosapods is directly triggered by the electrons and holes without involving radicals. The significantly improved photocatalytic activity can be attributed to effective charge separation and transport capability, which are verified by the photoelectrochemical and ultrafast transient absorption spectroscopy measurements.

Results and discussion

In a typical synthesis, Ag–CdS icosapods with an arm length of ~45 nm were well prepared according to our recent report with a slight modification (see the ESI for experimental details and Fig. S1†).[48] To prepare the Cu_2S icosapods, the as-obtained Ag–CdS icosapods were then dropped into a solution of CuI in acetonitrile/methanol (v/v, 4 : 1) at room temperature with ultrasonication. Transmission electron microscopy (TEM) and high-resolution transmission electron microscopy (HRTEM) images show that the morphology and size of the obtained products are well preserved with respect to the Ag–CdS icosapods, except that obvious cavities appeared in the center of the icosapods (Fig. 1a and b). The X-ray diffraction (XRD) pattern reveals that all diffraction peaks can be well matched with chalcocite Cu_2S, while the diffraction peaks ascribed to *fcc*-Ag in pristine Ag–CdS icosapods are absent (Fig. 1c). The measured lattice fringe of 0.34 nm can be assigned to the (002) plane of chalcocite Cu_2S (Fig. 1b, inset). The Ag cores may be oxidized or diffused outward to form hollow cavities during the cation exchange, which was also confirmed by scanning electron microscopy-energy dispersive X-ray spectrometry (SEM-EDX). As shown in Fig. 1d and Fig. S2a,† the Ag cannot be distinguished, and only Cu and S exist in the product with an atomic ratio of ~1.85, which is close to the stoichiometric value for Cu_2S. Furthermore, high-angle annular dark-field scanning transmission electron microscopy (HAADF-STEM) and the corresponding energy dispersive spectroscopy (EDS) elemental mappings show that the Cu and S are homogeneously distributed over the branches of the whole icosapods (Fig. 1e). The X-ray photoelectron spectroscopy (XPS) survey spectrum displays the existence of Cu and S elements in the Cu_2S icosapods (Fig. S3a†). In the high-resolution Cu 2p spectrum, the two fitted strong signals peaking at 952.7 and 932.9 eV can be ascribed to Cu^+ $2p_{1/2}$ and Cu^+ $2p_{3/2}$ of Cu_2S, whereas the other peaks located at around 954.4 and 934.4 eV can be assigned to Cu^{2+} $2p_{1/2}$ and Cu^{2+} $2p_{3/2}$ of the remnant copper oxide by oxidization, respectively (Fig. 1f). For the S 2p spectrum, two fitted peaks located at 163.0 and 161.8 eV can be ascribed to S^{2-} $2p_{1/2}$ and S^{2-} $2p_{3/2}$ of Cu_2S, respectively (Fig. S3b†).[49,50] All in all, the Cu_2S icosapods have been successfully prepared with high yield by cation exchange with the assistance of ultrasonication.

It is well known that $Cu_{2-x}S$ ($0 < x < 1$) nanocrystals with different morphologies are widely chosen as the host materials for the cation exchange reaction because of their fast Cu^+ diffusion and solvation capabilities with the introduction of alkyl phosphine according to the hard-soft acid-base theory.[51–54] Therefore, a variety of icosapods with tunable compositions can be easily obtained by the cation exchange of the Cu_2S icosapods with different metal ions (*i.e.*, Cd^{2+}, Zn^{2+}, Mn^{2+}, Co^{2+}, and Ni^{2+}). TEM and SEM images illustrate the corresponding

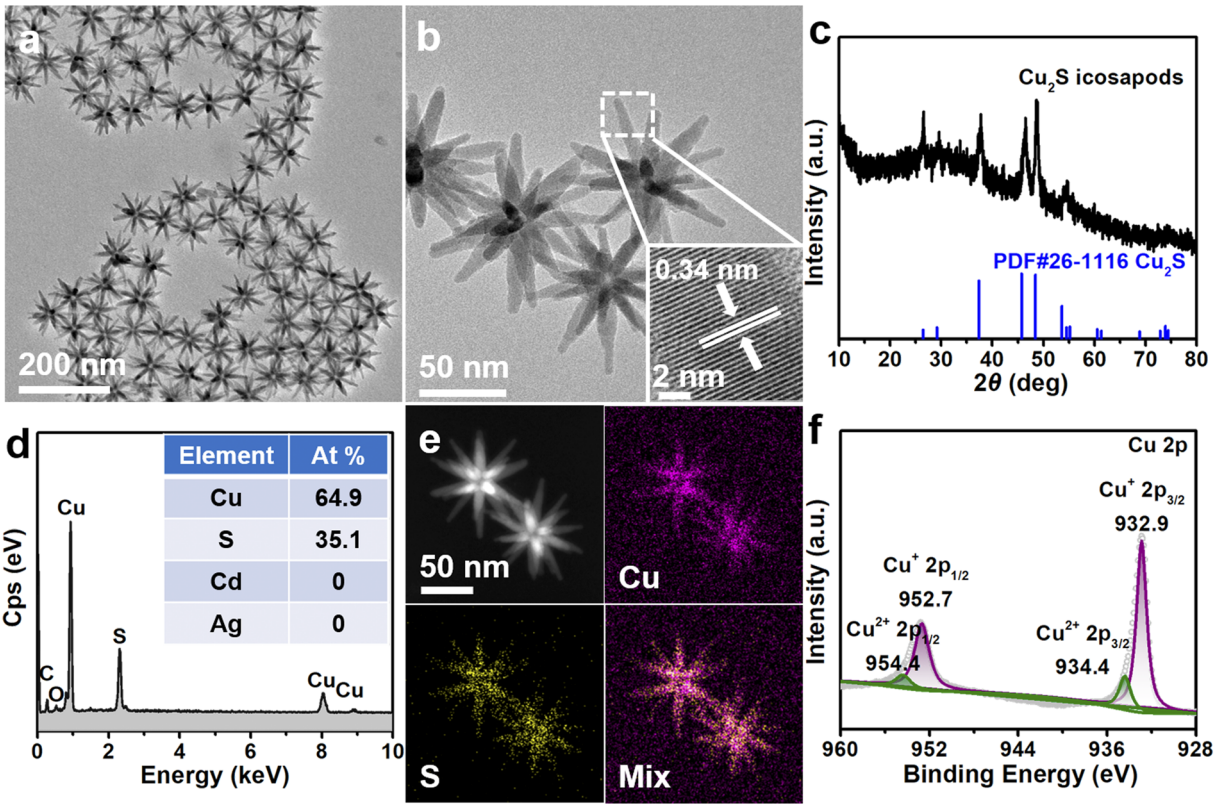

Fig. 1 (a) TEM and (b) HRTEM images of Cu_2S icosapods. The inset of b displays the HRTEM image taken from the white dashed square. (c) XRD pattern of the Cu_2S icosapods. The standard diffraction peaks for chalcocite Cu_2S (PDF#26-1116) are used as references. (d) SEM-EDX profile and the corresponding elemental contents (inset) of the Cu_2S icosapods. (e) HAADF-STEM image and the corresponding EDS elemental mappings of the Cu_2S icosapods. (f) High-resolution XPS spectrum of Cu 2p for the Cu_2S icosapods.

morphologies of the as-prepared five types of products, which intactly inherit the overall configuration of the Cu_2S icosapods (Fig. S4a1–e1† and Fig. S2b–f†). The XRD patterns confirm that the Cu_2S icosapods have been successfully transformed into the corresponding icosapods with wurtzite structures (CdS, ZnS, and MnS) and zinc blende structures (Co_9S_8 and Ni_3S_4), respectively (Fig. S4a4–e4†). The HRTEM images and fast Fourier transforms (FFTs) reveal the highly crystalline structure of the as-prepared icosapods (Fig. S4a2–e2†). The measured lattice fringes of 0.34 and 0.31 nm are consistent with the (002) planes of wurtzite CdS and ZnS, respectively (Fig. S4a2 and b2†). The FFT patterns show that the longitudinal directions of MnS, Co_9S_8, and Ni_3S_4 arms in icosapods are parallel to $[0001]_{wz}$, $[111]_{zb}$ and $[111]_{zb}$ directions, respectively (Fig. S4c2–e2†). The HAADF-STEM images and corresponding EDS elemental mappings were recorded where the corresponding metals and S were homogeneously overlapped in the finally yielded icosapods (Fig. S4a3–e3†). The XPS spectra of these five types of icosapods are shown in Fig. S5–S9,† verifying the successful preparation of the corresponding metal sulfide icosapods.

Furthermore, the as-obtained CdS icosapods can also be completely or partially cation exchanged with Pd^{2+}, by adjusting the feeding amount of the precursor, to get Pd_xS and CdS–Pd_xS icosapods, respectively. After the cation exchange reaction, the overall morphology of the Pd_xS and CdS–Pd_xS icosapods still remains the same (Fig. 2a and d) and shows a high degree of shape uniformity (Fig. S10†), but the crystal structure changes accordingly. The XRD pattern of the Pd_xS icosapods only displays a broad peak at around 40°, indicating the amorphous structure of the as-obtained Pd_xS icosapods (Fig. 2f, blue line). The HRTEM image of the Pd_xS branches shows the disordered arrangement without clear lattice fringes (Fig. 2b), and the selected area electron diffraction (SAED) pattern only displays diffusing rings, further confirming its amorphous structure (Fig. 2b, inset). The overview SEM-EDX profile reveals that the atomic ratio of Pd and S in Pd_xS icosapods is about 4.9 (Fig. S11a†). The HAADF-STEM image and the corresponding EDS elemental mappings of Pd_xS icosapods verify that Pd and S distribute homogeneously over the icosapods (Fig. 2c). The XPS spectrum of the Pd_xS icosapods indicates the existence of Pd^0 and Pd^{2+} (Fig. S11c†).[55–57] While the CdS icosapods undergo partial cation exchange with Pd^{2+}, only the tip areas of each arm have transformed into Pd_xS and the main trunk of the CdS arm still remains (Fig. 2d and e). The FFT pattern of the selected area (Fig. 2e, white dashed square) demonstrates that only one set of diffraction spots appeared for a single arm, while the FFT pattern from the tip area of the arm shows no obvious diffraction spots, indicating the amorphous structure of the Pd_xS tip. Moreover, the XRD pattern of the CdS–Pd_xS icosapods is in accordance with the hexagonal wurtzite CdS and no cubic Pd or

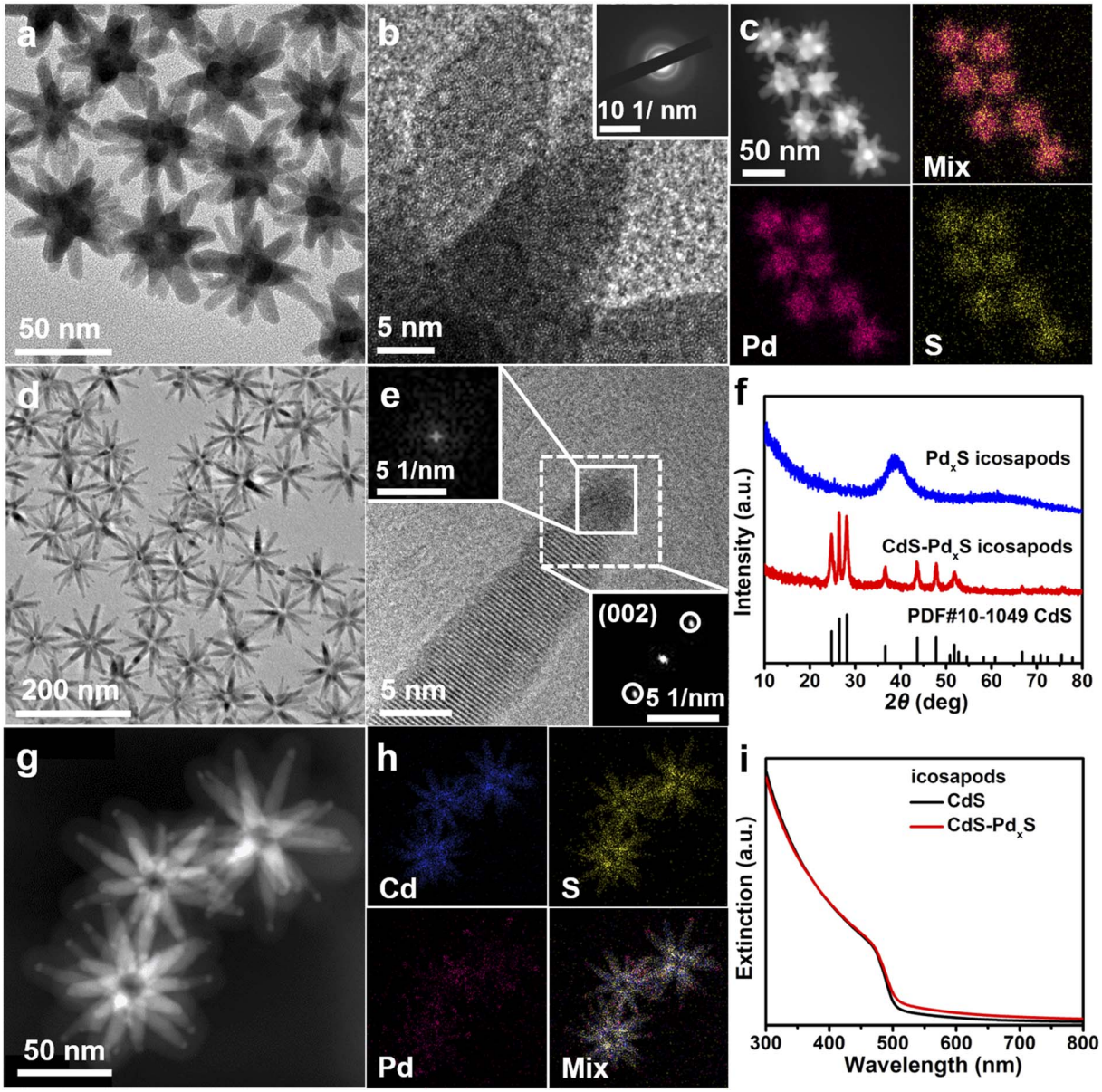

Fig. 2 TEM and HRTEM images of (a and b) Pd$_x$S and (d and e) CdS–Pd$_x$S icosapods, respectively. The inset of b shows the SEAD image of Pd$_x$S icosapods. The insets of (e) display FFT images taken from the selected squares. (c) HAADF-STEM image and the corresponding EDS elemental mappings of the amorphous Pd$_x$S icosapods. (f) XRD patterns of the Pd$_x$S and CdS–Pd$_x$S icosapods. (g) HAADF-STEM image and (h) the corresponding EDS elemental mappings of CdS–Pd$_x$S icosapods. (i) UV-vis extinction spectra of the CdS and CdS–Pd$_x$S icosapods.

Pd$_x$S crystal structure can be detected (Fig. 2f, red line). The HAADF-STEM image of CdS–Pd$_x$S icosapods illustrates clear contrast between the arms and the tips, and the corresponding EDS elemental mappings further confirm that the Pd and Cd elements are confined in the tip and trunk areas, respectively, while the S element distributes homogeneously over the whole icosapods (Fig. 2g and h). The atomic ratio of Pd in CdS–Pd$_x$S icosapods is 5.3% according to SEM-EDX (Fig. S12a†). The XPS spectra of CdS–Pd$_x$S icosapods are given in Fig. S12b–e,† revealing the similar valence states of each element compared with the aforementioned Pd$_x$S and CdS icosapods (Fig. S11† and S5†). As seen in Fig. 2i, the CdS and CdS–Pd$_x$S icosapods exhibit similar band edge absorption at around 485 nm in the UV-vis extinction spectrum.

The CdS–Pd$_x$S icosapods are expected to show excellent performance for photocatalytic organic transformations. Firstly, the icosapod structures are mainly composed of CdS, which possesses a suitable band gap (~2.4 eV) for strong visible light absorption. Secondly, the components of CdS and Pd$_x$S form lots of interfaces, which would accelerate the separation efficiency and transport of photogenerated carriers. Finally, due to the large specific surface area of the branched nanostructures and the low-coordinated Pd in amorphous Pd$_x$S tips, the oxidation and reduction reactions induced by holes and

electrons could proceed smoothly and effectively. As a proof-of-concept demonstration, upgrading oxidation of biomass-relevant alcohols into corresponding aldehydes coupled with H_2 evolution under visible-light irradiation (λ > 420 nm) was investigated by using the CdS–Pd_xS icosapods as the photocatalyst. The H_2 and corresponding liquid products were identified by gas chromatography spectrometry (GC) and gas chromatograph-mass spectrometry (GC-MS), respectively (Fig. S13–S20†). The UV-vis extinction spectra of different photocatalysts in Fig. 3a are shown in Fig. S21.† The dehydrogenation of BA into benzaldehyde (BZD) was initially carried out as a model photoreaction in an acetonitrile solution containing 0.1 mmol of BA and 10 mg of the photocatalysts, which was irradiated with a xenon lamp under a nitrogen atmosphere. As displayed in Fig. 3a, both Pd and Pd_xS nanoparticles don't show any activity for the dehydrogenation reaction after 2 h of illumination. Interestingly, the CdS–Pd_xS icosapods show a superior photoactivity compared with blank CdS icosapods and a physical mixture of CdS icosapods and Pd_xS nanoparticles with the same Pd content (Fig. 3a). The conversion and selectivity of BA on CdS–Pd_xS icosapods are up to 98.1% and 99.1%, respectively, which are 31.6 and 2.6 times higher than those on single CdS icosapods (Table 1, entry 1). Although the conversion of BA on the physical mixture is relatively moderate, many undesired products appeared and the selectivity is only 39.5%. Moreover, one-dimensional CdS–Pd_xS nanorods (NRs, Fig. S22†), which also possess a similar Pd atomic ratio, only show quite low conversion (43.1%) and good selectivity (94.0%), reflecting the distinct architecture superiority of the heterostructures. In this case, BA can be almost completely converted by CdS–Pd_xS NRs when the reaction time extends to 4 h, while the selectivity decreased to 90.0%. The interfacial electronic structures of the CdS–Pd_xS icosapods and nanorod photocatalysts have been measured by ultraviolet photoelectron spectroscopy (Fig. S23†). An apparent Schottky junction is formed in both CdS–Pd_xS samples due to very close Fermi levels of Pd_xS with respect to Pd NPs. In addition, the as-prepared CdS–Pd_xS icosapods and nanorod photocatalysts not only meet the reduction potential required for the conversion of H^+ to H_2, but also meet the oxidation potential of selective oxidation of BA to BAD. To evaluate the recyclability and durability of the CdS–Pd_xS icosapod photocatalysts, a recycling experiment has been performed, indicating a marginal loss in the photocatalytic performance even after four cycles (Fig. 3b). Impressively, the optimized H_2 evolution and AQY (calculated based on H_2) of the BA reforming on CdS–Pd_xS icosapods are measured to be 16.01 mmol g^{-1} h^{-1} and 31.4% at 420 nm, respectively, which is a competitive photocatalytic system for selective organic transformation integrated with H_2 evolution (Table S1†).

Next, the substrate scope of the CdS–Pd_xS icosapod system with regard to photocatalytic selective oxidation of many types of biomass-relevant alcohols has also been investigated. It is found that all aromatic and aromatic heterocyclic alcohols were oxidized smoothly to the corresponding aldehydes with excellent selectivity (>94.8%, Table 1, entries 1–7). However, in the

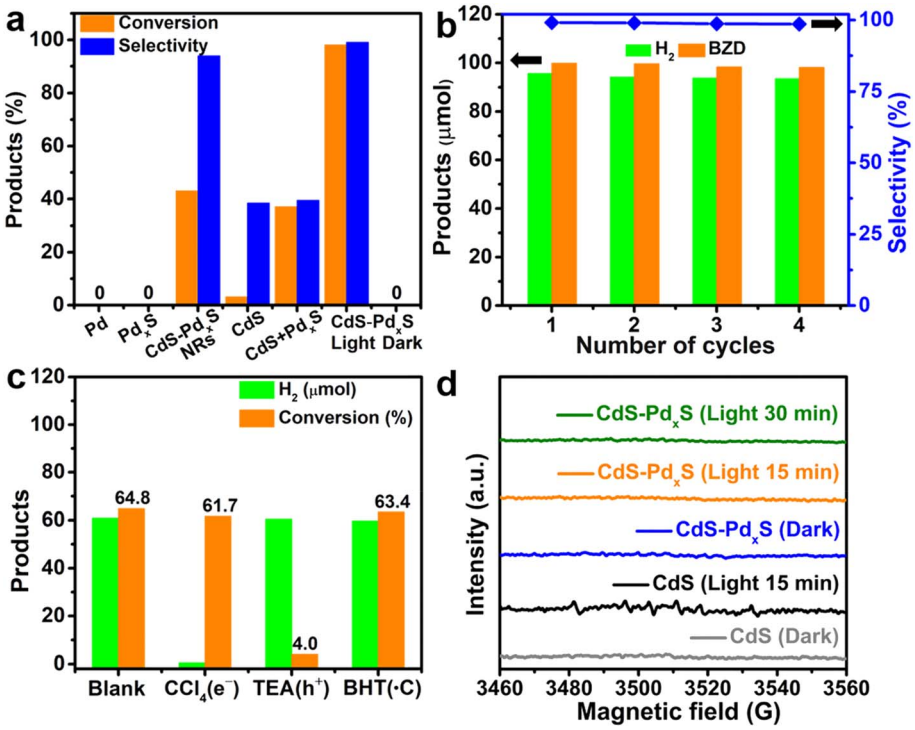

Fig. 3 (a) Photocatalytic oxidation performance of BA over Pd nanoparticles, Pd_xS nanoparticles, CdS–Pd_xS NRs, CdS icosapods, physical mixture of CdS icosapods and Pd_xS nanoparticles, and CdS–Pd_xS icosapods under visible-light irradiation (λ > 420 nm). (b) Photocatalytic recycling tests for the CdS–Pd_xS icosapods. (c) Quenching experiments with different reactive species photocatalyzed by the CdS–Pd_xS icosapods. (d) *In situ* EPR spectra in N_2 saturated CH_3CN solution with the addition of DMPO.

Table 1 Photocatalytic selective oxidation of biomass-relevant alcohols over CdS–Pd_xS icosapods under visible-light irradiation (λ > 420 nm)

Entry	Substrate	Product	Conversion (%)	Selectivity (%)	H_2 (μmol)	Reaction time (h)
1	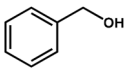	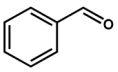	98.1	99.1	95.9	2
2	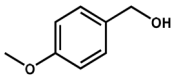	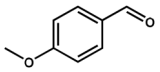	98.6	99.7	96.5	2
3	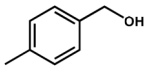	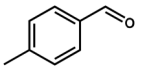	98.3	99.8	96.3	2
4	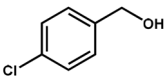	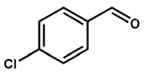	97.6	99.7	95.0	2.5
5	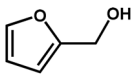	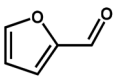	98.8	99.3	96.4	4
6	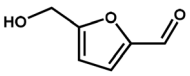	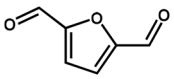	47.8	94.8	42.9	8
7	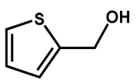	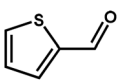	89.7	99.3	85.8	6
8	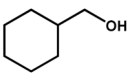	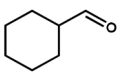	23.9	90.4	22.2	24

case of alicyclic alcohols, although their conversions are low, the selectivity of dehydrogenative products is still high (Table 1, entry 8). Notably, the molar ratio of all oxidation products (aldehydes) and the reduction product (H_2) is calculated to be nearly 1, implying a stoichiometric dehydrogenation reaction (Table 1, entries 1–8). The influence of the electronic effect of functional groups at the *para*-position on the photocatalytic oxidation of substituted benzylic alcohol by CdS–Pd_xS icosapods has also been observed. By taking unsubstituted BA as the reference, the aldehyde production rate is enhanced by introduction of electron-donating groups, *e.g.* $-OCH_3$ and $-CH_3$ (entries 2 and 3), while the installation of an electron-withdrawing group (–Cl, entry 4) can apparently suppress the reaction rate and the illumination time needs to be extended to 2.5 h to make the conversion up to 97%. It is worth mentioning that furfuryl alcohol (FA) and HMF, two kinds of most crucial biomass-derived platform chemicals, also show exciting conversion and selectivity into corresponding furfural and 2,5-diformylfuran over the photocatalyst (Table 1, entries 5 and 6). Specifically, under dark conditions, no transformation occurs for FA and HMF over the CdS–Pd_xS icosapods (Fig. S24†). However, the furfural is obtained with a conversion and selectivity of 98.8% and 99.3% after only 4 h of light irradiation, while the single materials of CdS icosapods are measured to be 1.5% and 13.2%, respectively. As for HMF, the formation of overoxidized products, such as 5-hydroxymethyl-2-furancarboxylic acid, 5-formyl-2-furancarboxylic acid, and 2, 5-furandicarboxylic acid, cannot be observed in our case over the CdS–Pd_xS icosapods within 8 h of illumination.[14,20] The conversion and selectivity are up to 47.8% and 94.8%, which are 59.8 and 2.6 times higher than those of CdS icosapods, respectively. Compared to the reported studies, the as-prepared CdS–Pd_xS icosapods exhibit excellent photoreforming performance over such biomass-derived intermediates (Table S1†).

To unveil the possible role of the reactive species and radical intermediates in the photoredox-catalyzed system, trapping experiments have been executed by taking BA transformation as an example (Fig. 3c). Because the selective oxidation of BA into BZD was carried out so quickly, the photocatalytic reactions implemented in an hour were monitored in the trapping experiments. As seen in Fig. 3c, the addition of tetrachloromethane (CCl_4) as an electron scavenger completely ceased the H_2 evolution, while the conversion efficiency of BA oxidation remained almost unchanged over CdS–Pd_xS icosapods. However, when triethylamine (TEA) was introduced for irreversible consumption of holes, the formation of BZD retarded apparently and the H_2 evolution kept up production. It is widely reported that the $^{\bullet}$CH(OH)Ph radical, which can be induced by the interaction between BA and h^+, is often considered the key intermediate for selective photo-oxidation of alcohol into aldehyde.[58,59] Therefore, butylated hydroxytoluene (BHT), a commonly used carbon-centered free radical trapping reagent, was added to verify whether $^{\bullet}$CH(OH)Ph radicals are involved in the photocatalytic process.[59] Clearly, both the conversion of BA and H_2 evolution remain, suggesting the simultaneous participation of electrons and holes for BZD and H_2 production instead of $^{\bullet}$CH(OH)Ph radicals. Furthermore, the carbon-centered free radicals have been further explored by the

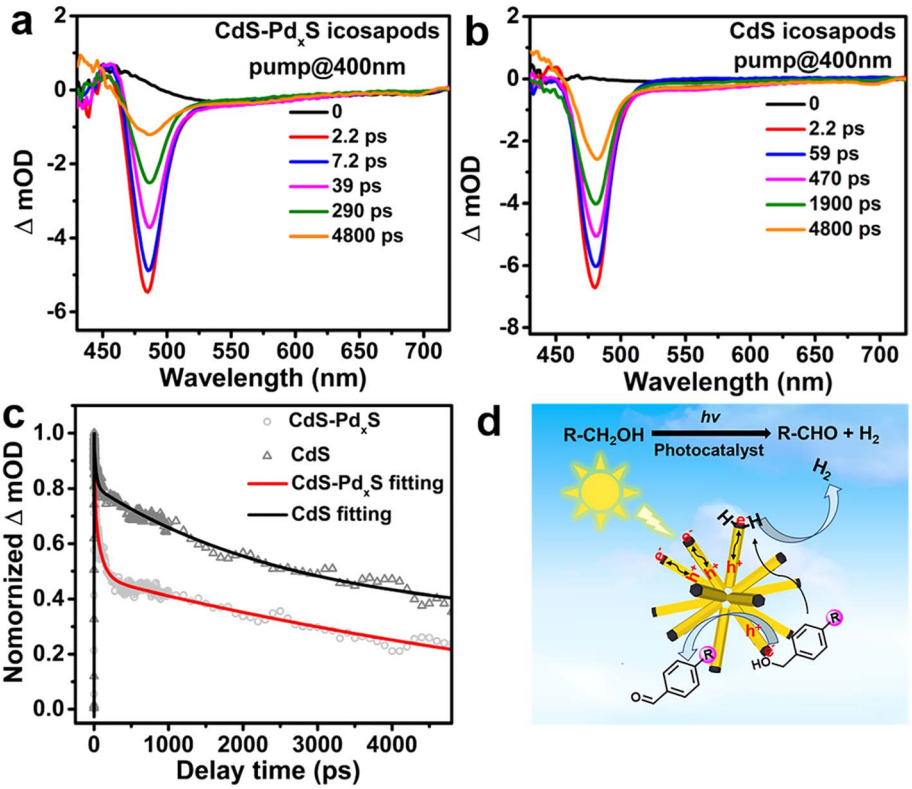

Fig. 4 TA spectra of the (a) CdS–Pd$_x$S and (b) CdS icosapods at different delay times with 400 nm excitation, respectively. (c) Comparison of 1Σ exciton bleach recovery kinetics of the CdS–Pd$_x$S (at 484 nm) and CdS icosapods (at 480 nm) when excited at 400 nm. (d) Proposed possible photocatalytic mechanism for selective oxidation of biomass-relevant alcohols into corresponding aldehydes integrated with H_2 evolution over the CdS–Pd$_x$S icosapods under visible-light irradiation.

in situ EPR measurements with 5,5-dimethyl-1-pyrroline *N*-oxide (DMPO) as the spin-trapping regent to gain more information on the radical intermediate mechanism of the reaction (Fig. 3d). Under the dark and light irradiation conditions, no obvious signal appeared over the solution, manifesting no carbon-centered free radicals involved in the photoreaction. Otherwise, the ˙CH(OH)Ph radical is gradually evolved over CdS icosapods with illumination and eventually trapped by DMPO, as evidenced by the characteristic signal peaks belonging to the DMPO-CH(OH)Ph adduct.[58,59]

Based on the above results, the photoreforming of biomass-relevant alcohols can be proceeded by direct participation of the photo-generated electrons and holes in the CdS–Pd$_x$S icosapods. To deeply explore the origin of striking photocatalytic activity of the CdS–Pd$_x$S icosapods, the separation and transport dynamics of photogenerated charges were systematically surveyed. First, the photoelectrochemical (PEC) experiment reveals that the transient photocurrent response for CdS–Pd$_x$S icosapods is much higher with respect to that of the single component of CdS icosapods, indicating the importance of construction of heterostructures to enhance the photocatalytic activity (Fig. S25†). Moreover, ultrafast transient absorption spectroscopy (TA) was used to uncover the photo-excited charge dynamics of the CdS–Pd$_x$S and CdS icosapods under 400 nm laser pumping. The fluence dependence of the time-resolved transient absorption measurement indicates that the feature is derived from one-photon excitation (Fig. S26†). As shown in Fig. 4a and b, the CdS–Pd$_x$S and CdS icosapods show similar 1Σ exciton bleach signals at around 480 nm, originating from the state filling of the conduction band $1\sigma_e$ electron level for CdS.[60] The corresponding 1Σ exciton bleach recovery kinetics within 4.8 ns for both icosapods clearly demonstrate that the kinetics recovery process becomes significantly faster over the CdS–Pd$_x$S icosapods, indicating the enhanced depopulation rate of conduction band electrons in the icosapods (Fig. S27† and 4c). As reported in the literature, the CdS nanorods with a small amount of Pd$_x$S tips would favor electron transfer in heterostructures.[55,56] Similarly, the photogenerated electrons would immediately transfer from the CdS trunk to the amorphous Pd$_x$S tip in the CdS–Pd$_x$S icosapods, instead of the direct recombination of charge carriers or possible charge trapping by the defects for the CdS icosapods.[61–63] In this way, spatially separated photogenerated electrons and holes in CdS–Pd$_x$S icosapods offer more opportunities to separately participate in the corresponding photocatalytic reactions. Therefore, a possible photocatalytic mechanism for selective oxidation of biomass-relevant alcohols into corresponding aldehydes coupled with H_2 evolution over the CdS–Pd$_x$S icosapods is depicted in Fig. 4d. Initially, the photoinduced carriers are generated in CdS under light illumination. Then, the photogenerated electrons promptly transfer to the domains of Pd$_x$S tips, while the holes still localize at CdS trunks. The protons

from–OH bonds of the biomass-relevant alcohols, which pre-adsorb on the Pd_xS tips of the CdS–Pd_xS icosapods, can be reduced by photoinduced electrons and thus form a Pd–H hydride and an alkoxide anion. Subsequently, the alkoxide anion is immediately photooxidized into corresponding aldehyde products by the photoinduced holes in the CdS trunks and releases another Pd–H hydride simultaneously. Finally, two Pd–H hydrides generate H_2 in the Pd_xS tips (Fig. 4d).

Conclusion

In summary, a series of highly branched metal sulfides and heterostructured icosapods based on them with delicate architecture and tunable compositions have been successfully produced by consecutive cation exchange. All obtained icosapods exhibit high symmetry and integral structure homogeneity. As a proof of concept, the CdS–Pd_xS icosapods displays remarkably enhanced photocatalytic activity for selective oxidation of biomass-relevant alcohols, including aromatic and aromatic heterocyclic alcohols, into corresponding aldehydes (Sel. >94.8%) coupled with H_2 evolution. Impressively, the AQY of the benzyl alcohol reforming on the CdS–Pd_xS icosapods can be achieved as high as 31.4% at 420 nm. The photoreforming of biomass-relevant alcohols is found to be followed by direct participation of the photo-generated electrons and holes in the CdS–Pd_xS icosapods, rather than the involvement of radicals. The superior photocatalytic performance of the CdS–Pd_xS icosapods results from the enhanced charge separation capability and the fast electron migration in the heterostructured icosapods. We believe that this work will inspire further study on the controllable construction of heterostructures with well-defined architectures and explore their photocatalytic performance for organic molecule activation and transformation.

Data availability

The data that support the findings of this study are available in the main text and the ESI.†

Author contributions

X.-J. W., F. C. and M. D. supervised the project. X.-J. W. and D. X. conceived the idea. D. X. carried out the synthesis of the materials. D. X., Y. M., L. Z., and H. Z. performed HRTEM measurements. D. X. collected HAADF and EDS elemental mapping data. D. X., C.-L. T., and F.-Y. G. contributed to UV-vis and XRD characterization. X.-J. W., F. C. and D. X. wrote the manuscript. All authors discussed the experimental results.

Conflicts of interest

The authors declare no conflict of interest.

Acknowledgements

This work was supported by the National Natural Science Foundation of China (22271142, 21871129 and 21902079), Natural Science Foundation of Jiangsu Province of China (BK20190724), and the "Innovation & Entrepreneurship Talents Plan" of Jiangsu Province.

Notes and references

1 H. Li, F. Qin, Z. Yang, X. Cui, J. Wang and L. Zhang, *J. Am. Chem. Soc.*, 2017, **139**, 3513–3521.
2 Y.-H. Li, F. Zhang, Y. Chen, J.-Y. Li and Y.-J. Xu, *Green Chem.*, 2020, **22**, 163–169.
3 P. Zhou, L. Jiang, F. Wang, K. Deng, K. Lv and Z. Zhang, *Sci. Adv.*, 2017, **3**, 1601945–1601955.
4 M. Kaur and C. M. Nagaraja, *ACS Sustainable Chem. Eng.*, 2017, **5**, 4293–4303.
5 H. Liu, C. Xu, D. Li and H.-L. Jiang, *Angew. Chem., Int. Ed.*, 2018, **57**, 5379–5383.
6 C. Han, Y. H. Li, J. Y. Li, M. Y. Qi, Z. R. Tang and Y.-J. Xu, *Angew. Chem., Int. Ed.*, 2021, **60**, 7962–7970.
7 W. Zhang, E. Fernández-Fueyo, Y. Ni, M. van Schie, J. Gacs, R. Renirie, R. Wever, F. G. Mutti, D. Rother, M. Alcalde and F. Hollmann, *Nat. Catal.*, 2017, **1**, 55–62.
8 N. Luo, T. Montini, J. Zhang, P. Fornasiero, E. Fonda, T. Hou, W. Nie, J. Lu, J. Liu and M. Heggen, *Nat. Energy*, 2019, **4**, 575–584.
9 D. Li, Y. Zhao, Y. Miao, C. Zhou, L. P. Zhang, L.-Z. Wu and T. Zhang, *Adv. Mater.*, 2022, **34**, 2207793–2207799.
10 M. Y. Qi, M. Conte, M. Anpo, Z. R. Tang and Y.-J. Xu, *Chem. Rev.*, 2021, **121**, 13051–13085.
11 L.-M. Zhao, Q.-Y. Meng, X.-B. Fan, C. Ye, X.-B. Li, B. Chen, V. Ramamurthy, C.-H. Tung and L.-Z. Wu, *Angew. Chem., Int. Ed.*, 2017, **56**, 3020–3024.
12 D. Jiang, X. Chen, Z. Zhang, L. Zhang, Y. Wang, Z. Sun, R. M. Irfan and P. Du, *J. Catal.*, 2018, **357**, 147–153.
13 X. Sun, X. Luo, X. Zhang, J. Xie, S. Jin, H. Wang, X. Zheng, X. Wu and Y. Xie, *J. Am. Chem. Soc.*, 2019, **141**, 3797–3801.
14 T. Xia, W. Gong, Y. Chen, M. Duan, J. Ma, X. Cui, Y. Dai, C. Gao and Y. Xiong, *Angew. Chem., Int. Ed.*, 2022, **61**, 202204225–202204230.
15 S. C. Jensen, S. B. Homan and E. A. Weiss, *J. Am. Chem. Soc.*, 2016, **138**, 1591–1600.
16 A. C. Poulose, G. Zoppellaro, I. Konidakis, E. Serpetzoglou, E. Stratakis, O. Tomanec, M. Beller, A. Bakandritsos and R. Z. boril, *Nat. Nanotechnol.*, 2022, **17**, 485–492.
17 J. L. DiMeglio and B. M. Bartlett, *Chem. Mater.*, 2017, **29**, 7579–7586.
18 F. Raza, J. H. Park, H.-R. Lee, H.-I. Kim, S.-J. Jeon and J.-H. Kim, *ACS Catal.*, 2016, **6**, 2754–2759.
19 Z. Chai, T.-T. Zeng, Q. Li, L.-Q. Lu, W.-J. Xiao and D. Xu, *J. Am. Chem. Soc.*, 2016, **138**, 10128–11013.
20 G. Han, Y.-H. Jin, R. A. Burgess, N. E. Dickenson, X.-M. Cao and Y. Sun, *J. Am. Chem. Soc.*, 2017, **139**, 15584–15587.
21 L. Marzo, S. K. Pagire, O. Reiser and B. König, *Angew. Chem., Int. Ed.*, 2018, **57**, 10034–10072.
22 X.-B. Li, C.-H. Tung and L.-Z. Wu, *Nat. Rev. Chem*, 2018, **2**, 160–173.
23 J.-Y. Li, Y.-H. Li, M.-Y. Qi, Q. Lin, Z.-R. Tang and Y.-J. Xu, *ACS Catal.*, 2020, **10**, 6262–6280.

24 L. Xiong and J. Tang, *Adv. Energy Mater.*, 2021, **11**, 2003216–2003234.
25 K. Sun, Q.-Y. Lv, X.-L. Chen, L.-B. Qu and B. Yu, *Green Chem.*, 2021, **23**, 232–248.
26 Y. Li, C. Zhang, T. T. Zhuang, Y. Lin, J. Tian, X. Y. Qi, X. Li, R. Wang, L. Wu, G. Q. Liu, T. Ma, Z. He, H. B. Sun, F. Fan, H. Zhu and S.-H. Yu, *J. Am. Chem. Soc.*, 2021, **143**, 7013–7020.
27 Z. K. Xin, Y. J. Gao, Y. Gao, H. W. Song, J. Zhao, F. Fan, A. D. Xia, X. B. Li, C.-H. Tung and L.-Z. Wu, *Adv. Mater.*, 2022, **34**, 2106662–2106670.
28 X.-B. Li, Z.-K. Xin, S.-G. Xia, X.-Y. Gao, C.-H. Tung and L.-Z. Wu, *Chem. Soc. Rev.*, 2020, **49**, 9028–9056.
29 F. Li, Y. Wang, J. Du, Y. hu, C. Xu and L. Sun, *Appl. Catal., B*, 2018, **225**, 258–263.
30 G. Han, T. Yan, W. Zhang, Y. C. Zhang, D. Y. Lee, Z. Cao and Y. Sun, *ACS Catal.*, 2019, **9**, 11341–11349.
31 H. Hao, L. Zhang, W. Wang, S. Qiao and X. Liu, *ACS Sustainable Chem. Eng.*, 2019, **7**, 10501–10508.
32 F. Raza, D. Yim, J. H. Park, H.-I. Kim, S.-J. Jeon and J.-H. Kim, *J. Am. Chem. Soc.*, 2017, **139**, 14767–14774.
33 Y. Huang, C. Liu, M. Li, H. Li, Y. Li, R. Su and B. Zhang, *ACS Catal.*, 2020, **10**, 3904–3910.
34 S. Liu, M. Yang, Z. Tang and Y. Xu, *Nanoscale*, 2014, **6**, 7193–7198.
35 C. Han, Z. Chen, N. Zhang, J. Colmenares and Y. Xu, *Adv. Funct. Mater.*, 2015, **25**, 221–229.
36 Y. Sung, J. Lim, J. H. Koh, L. J. Hill, B. K. Min, J. Pyun and K. Char, *CrystEngComm*, 2015, **17**, 8423–8427.
37 M. Karakus, Y. Sung, H. I. Wang, Z. Mics, K. Char, M. Bonn and E. Cánovas, *J. Phys. Chem. C*, 2017, **121**, 13070–13077.
38 S. W. Tong, N. Mishra, C. L. Su, V. Nalla, W. Wu, W. Ji, J. Zhang, Y. Chan and K. P. Loh, *Adv. Funct. Mater.*, 2014, **24**, 1904–1910.
39 H. Lee, J. Lim, J. Song, H. Heo, K. An, J. Kim, S. Lee, K. Char, H. J. Song and C. Lee, *Nanotechnology*, 2019, **30**, 065401–065410.
40 X. Li, Y. Zhang, L. Zhai, C.-L. Tao, D. Xu, Z. Mu, M. Ding and X.-J. Wu, *Angew. Chem., Int. Ed.*, 2021, **60**, 3475–3480.
41 M. J. Bierman and S. Jin, *Energy Environ. Sci.*, 2009, **2**, 1050–1059.
42 C. Cheng and H. J. Fan, *Nano Today*, 2012, **7**, 327–343.
43 X. Li, J. Yu and M. Jaroniec, *Chem. Soc. Rev.*, 2016, **45**, 2603–2636.
44 N. Mishra, V. G. Vasavi Dutt and M. P. Arciniegas, *Chem. Mater.*, 2019, **31**, 9216–9242.
45 A. Nawaz, S. Goudarzi, M. A. Asghari, S. Pichiah, G. S. Selopal, F. Rosei, Z. M. Wang and H. Zarrin, *ACS Appl. Nano Mater.*, 2021, **4**, 11323–11352.
46 A. Fiore, R. Mastria, M. G. Lupo, G. Lanzani, C. Giannini, E. Carlino, G. Morello, M. De Giorgi, Y. Li, R. Cingolani and L. Manna, *J. Am. Chem. Soc.*, 2009, **131**, 2274–2282.
47 S. Deka, K. Miszta, D. Dorfs, A. Genovese, G. Bertoni and L. Manna, *Nano Lett.*, 2010, **10**, 3770–3776.
48 L. Zhai, S. T. Gebre, B. Chen, D. Xu, J. Chen, Z. Li, Y. Liu, H. Yang, C. Ling, Y. Ge, W. Zhai, C. Chen, L. Ma, Q. Zhang, X. Li, Y. Yan, X. Huang, L. Li, Z. Guan, C.-L. Tao, Z. Huang, H. Wang, J. Liang, Y. Zhu, C.-S. Lee, P. Wang, C. Zhang, L. Gu, Y. Du, T. Lian, H. Zhang and X.-J. Wu, *Nat. Commun.*, 2023, **14**, 2538–2547.
49 W. Y. Wu, S. Chakrabortty, A. Guchhait, G. Y. Z. Wong, G. K. Dalapati, M. Lin and Y. Chan, *Chem. Mater.*, 2016, **28**, 9132–9913.
50 Q. Peng, S. Zhang, H. Yang, B. Sheng, R. Xu, Q. Wang and Y. Yu, *ACS Nano*, 2020, **14**, 6024–6033.
51 D. H. Son, S. M. Hughes, Y. Yin and A. Paul Alivisatos, *Science*, 2004, **306**, 1009–1012.
52 J. L. Fenton, B. C. Steimle and R. E. Schaak, *Science*, 2018, **360**, 513–517.
53 B. C. Steimle, J. L. Fenton and R. E. Schaak, *Science*, 2020, **367**, 418–442.
54 Z. Li, M. Saruyama, T. Asaka, Y. Tatetsu and T. Teranishi, *Science*, 2021, **373**, 332–337.
55 Y. Shemesh, J. E. Macdonald, G. Menagen and U. Banin, *Angew. Chem., Int. Ed.*, 2011, **50**, 1185–1221.
56 L. L. Long, A. Y. Zhang, Y. X. Huang, X. Zhang and H. Q. Yu, *J. Mater. Chem. A*, 2015, **3**, 4301–4306.
57 C. Du, P. Li, F. Yang, G. Cheng, S. Chen and W. Luo, *ACS Appl. Mater. Interfaces*, 2018, **10**, 753–761.
58 Y. H. Li, M. Y. Qi, Z. R. Tang and Y.-J. Xu, *J. Phys. Chem. C*, 2022, **126**, 1872–1880.
59 Z. Zhu, H. Huang, L. Liu, F. Chen, N. Tian, Y. Zhang and H. Yu, *Angew. Chem., Int. Ed.*, 2022, **61**, e202203519.
60 K. Wu, W. E. Rodríguez-Córdoba, Y. Yang and T. Lian, *Nano Lett.*, 2013, **13**, 5255–5263.
61 K. Wu, Y. Du, H. Tang, Z. Chen and T. Lian, *J. Am. Chem. Soc.*, 2015, **137**, 10224–10230.
62 K. Wu, H. Zhu, Z. Liu, W. Rodriguez-Cordoba and T. Lian, *J. Am. Chem. Soc.*, 2012, **134**, 10337–10340.
63 J. K. Utterback, A. N. Grennell, M. B. Wilker, O. M. Pearce, J. D. Eaves and G. Dukovic, *Nat. Chem.*, 2016, **8**, 1061–1066.